Inherited weak topological insulator signatures in the topological hourglass semimetal Nb_3XTe_6 (X = Si, Ge)

Q. Wan,[1,*] T. Y. Yang,[1,*] S. Li,[2] M. Yang,[3,4] Z. Zhu,[5] C. L. Wu,[1] C. Peng,[1] S. K. Mo,[1] W. Wu,[2] Z. H. Chen,[6] Y. B. Huang,[6] L. L. Lev,[7,8] V. N. Strocov,[7] J. Hu,[9] Z. Q. Mao,[10] Hao Zheng,[5] J. F. Jia,[5] Y. G. Shi,[3,4,11] Shengyuan A. Yang,[2] and N. Xu[1,†]

[1]*Institute of Advanced Studies, Wuhan University, Wuhan 430072, China*
[2]*Research Laboratory for Quantum Materials, Singapore University of Technology and Design, Singapore 487372, Singapore*
[3]*Beijing National Laboratory for Condensed Matter Physics and Institute of Physics, Chinese Academy of Sciences, Beijing 100190, China*
[4]*School of Physical Sciences, University of Chinese Academy of Sciences, Beijing 100190, China*
[5]*Key Laboratory of Artificial Structures and Quantum Control (Ministry of Education), Shenyang National Laboratory for Materials Science, School of Physics and Astronomy, Shanghai Jiao Tong University, 800 Dongchuan Road, Shanghai 200240, China*
[6]*Shanghai Synchrotron Radiation Facility, Shanghai Advanced Research Institute, Chinese Academy of Sciences, Shanghai 201204, China*
[7]*Swiss Light Source, Paul Scherrer Institut, CH-5232 Villigen PSI, Switzerland*
[8]*Moscow Institute of Physics and Technology, 9, Institutskiy lane, Dolgoprudny, Moscow region 141701, Russia*
[9]*Department of Physics, University of Arkansas, Fayetteville, Arkansas 72701, USA*
[10]*Department of Physics, Pennsylvania State University, University Park, Pennsylvania 16803, USA*
[11]*Songshan Lake Materials Laboratory, Dongguan, Guangdong 523808, China*

(Received 16 December 2020; revised 30 January 2021; accepted 17 March 2021; published 6 April 2021)

Using spin-resolved and angle-resolved photoemission spectroscopy and first-principles calculations, we have identified bulk band inversion and the spin-polarized surface state evolved from a weak topological insulator (TI) phase in van der Waals materials Nb_3XTe_6 (X = Si, Ge). The fingerprints of weak TIs homologically emerge with hourglass fermions as multinodal chains composed by the same pair of valence and conduction bands gapped by spin-orbit coupling. The unique topological state, with a pair of valence and conduction bands encoding both weak TI and hourglass semimetal nature, is essential and guaranteed by nonsymmorphic symmetry. It is distinct from TIs studied previously based on band inversions without symmetry protections.

DOI: 10.1103/PhysRevB.103.165107

I. INTRODUCTION

The topological property of wave functions is a key characterization of quantum materials [1–5]. Novel boundary states provide an observable signature of the nontrivial topological invariant of wave functions, and topological phase transitions are accompanied with modifications of boundary states. From the band theory point of view, band inversion [Figs. 1(a) and 1(b)] plays a critical role in the formation of a topological state. In a topological insulator (TI) [6–16], spin-orbit coupling (SOC) opens a bulk hybridization gap between the inverted bands, and Dirac surface states emerge in the gap with spin-momentum locking [Fig. 1(c)]. Benefiting from specific crystalline symmetries, nodes can survive within the bulk hybridization gap [Fig. 1(d)] and define topological semimetals (TSMs) [17–37]. Tuning the hopping term, SOC, on-site, and long-range Coulomb interactions, etc., topological phase transitions can be realized by removing the band inversion without changing symmetry [38–40], as described in Fig. 1(b). However, the wave function simultaneously embedding multiple types of topological phases is elusive and the properties of such state are unknown.

Here, we unveil a unique topological phase hosting both weak TI and hourglass TSM fingerprints in van der Waals (vdW) materials, Nb_3XTe_6 (X = Si, Ge). It is evolved from SOC gapped multinodal chains composed by the same pair of valence and conduction bands. Combining bulk-sensitive soft x-ray angle-resolved photoemission spectroscopy (SX ARPES), spin-resolved ARPES with surface-sensitive vacuum ultraviolet (VUV) light, and first-principles calculations, we uncover bulk band inversion and spin-polarized topological surface states induced by a weak TI phase with a unique topological invariant $Z_2 = \{0; 110\}$. The weak TI signatures are inherited as hourglass nodes close the hybridization gap as imposed by nonsymmorphic symmetry. We further demonstrate that the topological phase in Nb_3XTe_6 is based on a band inversion guaranteed by nonsymmorphic symmetry, which, in contrast to TI based on band inversion without symmetry protection as depicted in Figs. 1(a)–1(c), is essential and cannot be removed without breaking the nonsymmorphic

*These authors contributed equally to this work.
†nxu@whu.edu.cn

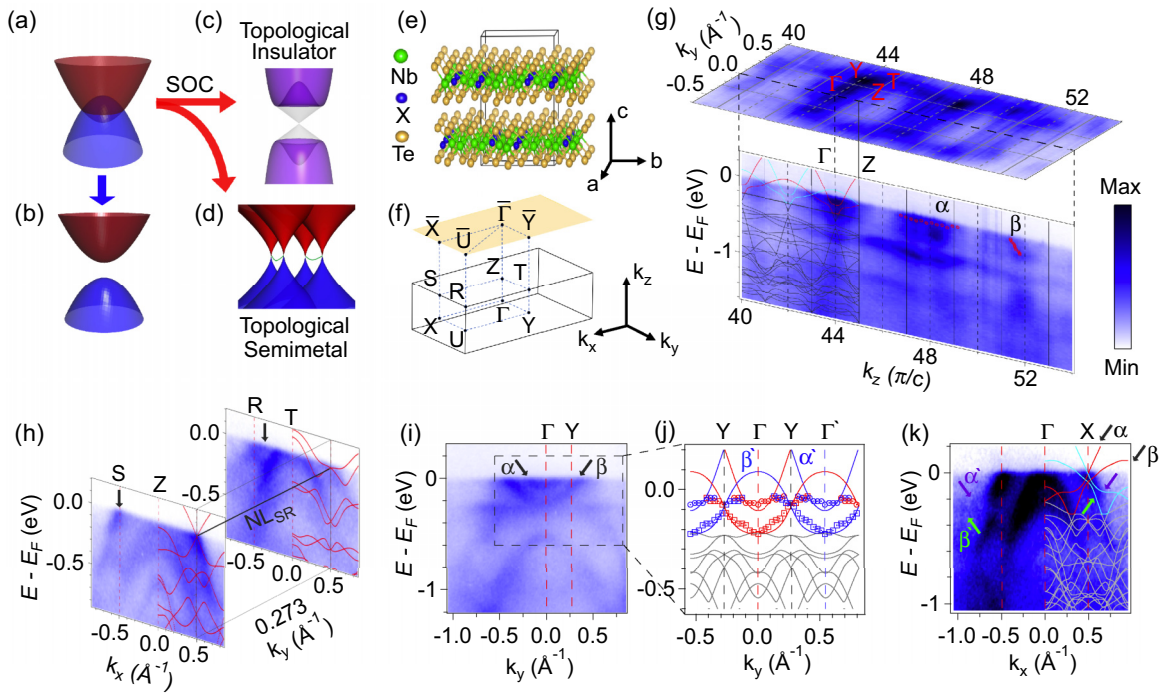

FIG. 1. (a), (b) Band structures with and without band inversion, respectively, when spin-orbit coupling (SOC) is not taken into account. (c), (d) SOC induced topological insulator and topological semimetal, respectively. (e) Crystal structure of Nb_3XTe_6. (f) Bulk and surface Brillouin zone with the high-symmetry points indicated. (g) Bulk band structure of Nb_3SiTe_6. The red symbols are extracted band dispersions. (h) Photoemission intensity plot along the *Z*-*S* and *T*-*R* directions. The black line represents the Dirac nodal line from calculations. (i), (j) Photoemission intensity plot along the Γ-*Y* direction. The red symbols indicate the extracted band structure and the blue ones are the same as the red symbols but shifted by $2\pi/b$. (k) Photoemission intensity plot along the Γ-*X* direction. The calculations without SOC are appended for a direct comparison in (g), (h), (j), (k). The red and blue lines in calculations in (g), (j), (k) represent bands near E_F with and without observable spectra weight in ARPES measurements, respectively.

symmetry. Our results not only realize a unique topological phase hosting distinctions of both weak TI and TSM phases by the same group of valence and conduction bands, but also provide a striking vdW material platform for fine-tuning the topological states, bulk/surface hourglass fermions, and their interplay with multiple parameters including thickness and Si/Ge stoichiometry.

Nb_3XTe_6 belongs to a vdW material family, $Nb_{2n+1}XTe_{4n+2}$, with crystal structure and Brillouin zones (BZ) shown in Figs. 1(e) and 1(f), respectively. In addition to the time-reversal symmetry T and inversion symmetry P, there are two glide mirror planes perpendicular to the x and y directions,

$$\widetilde{M}_x(x,y,z) \to (-x+1/2, y+1/2, z+1/2) \text{ and } \widetilde{M}_y(x,y,z) \to (x+1/2, -y+1/2, z),$$

respectively, characterizing the nonsymmorphic feature of the system. SOC strength in Nb_3XTe_6 is considerably strong due to the heavy Nb atoms. Previous theoretical study [41] predicts bulk hourglass fermions, with transport and ARPES evidences reported in a sister compound Ta_3SiTe_6 [42–44]. The system exhibits multiple methods for controlling the electronic and topological properties. Few-layer Nb_3SiTe_6 flakes have been successfully fabricated and enhanced electron coherence was reported [45]. By fine-tuning stoichiometry, directional massless Dirac fermions have been achieved in $NbSi_{0.45}Te_2$ with one-dimensional (1D) long-range order [46].

II. EXPERIMENTAL AND COMPUTATIONAL DETAILS

The Nb_3SiTe_6 single crystals were synthesized with a mixture of Nb, Si, and Te at a molar ratio of 3:1:6 using chemical vapor transport. During growth of Nb_3SiTe_6 the temperature was set at 950 °C and 850 °C, respectively, for the hot and cold ends of the double zone tube furnace. Single crystals of Nb_3GeTe_6 were grown by a solid-state reaction method. A mixture of Nb, Ge and Te at a molar ratio of 3:1:6 was pulverized, pressed into a pellet, placed in an alumina crucible, and then sealed in a highly evacuated quartz tube. After that, the tube was heated to 1100 °C for 10 h and slowly cooled down to 650 °C at a rate of 2 °C/h.

Clean surfaces for ARPES measurements were obtained by cleaving samples *in situ* in a vacuum greater than 5×10^{-11} Torr. VUV and SX-ARPES experiments were performed at Dreamline of the Shanghai Synchrotron Radiation Facility and SX-ARPES end station of the ADRESS beamline at the Swiss Light Source, Paul Scherrer Institute, Switzerland [47], respectively. Spin-resolved ARPES measurements were done with a home-designed ARPES facility equipped a very low energy electron diffraction (VLEED) spin detector, with a Sherman function of $S = 0.27$ used to generate the measured spin polarizations.

First-principles calculations were performed within the framework of density functional theory using the Perdew-Burke-Ernzerhof type [48] generalized gradient approximation for the exchange correlation functional as implemented

in the Vienna *ab initio* simulation package [49–51]. The BZ was sampled with Γ-centered k mesh of size $8 \times 5 \times 4$, and the cutoff energy was set as 350 eV. The energy and force convergence criteria were set to be 10^{-5} eV and 0.01 eV/Å, respectively. The van der Waals (vdW) corrections have been taken into account with the approach of Dion *et al.* [52]. The surface states were calculated by constructing the maximally localized Wannier functions [53,54] and by using the iterative Green's function method [55,56] as implemented in the WANNIERTOOLS package [57].

III. RESULTS

Figure 1(g) shows the ARPES spectra of Nb_3SiTe_6 acquired with $h\nu = 300$–570 eV. A k_z dispersive feature confirms the bulk origin of the photoelectron intensity in SX-ARPES measurements, due to the increase of the photoelectron mean free path compared to the VUV energy range [58]. A heavy band (named as α) and a light band (named as β) are resolved along the Γ-Z direction. Compared to calculations, they are visible in every other BZ due to a photoemission selection rule [59–61] related to nonsymmorphic symmetry $\widetilde{M}_x$ in Nb_3SiTe_6. Similarly, we observe a single branch of Dirac-cone-like dispersion along the Z-S direction in Fig. 1(h) due to $\widetilde{M}_y$. Off of the photoemission scattering plan, the selection rule is not strictly applied and both branches of Dirac-cone-like dispersions are visible along the T-R direction. Our results suggest a quasi-1D Dirac-cone-like dispersion along the S-R direction, consistent with the nodal line along the S-R high-symmetry line (NL_{SR}) protected by the interplay of $\tilde{M}_x$, $T\tilde{M}_y$, and PT, as indicated by the calculations without SOC [black line in Fig. 1(h)].

Furthermore, we observe multiple band inversions between the α and β bands, forming two kinds of nodal chains with finite and infinite length, respectively, if ignoring SOC. Along the Γ-Y direction [Figs. 1(i) and 1(j)], besides the α and β bands in the first BZ [red marks in Fig. 1(j)], the α' and β' bands are expected in the second BZ [blue marks in Fig. 1(j)] with zero spectra weight due to selection rule related to $\widetilde{M}_x$. Because both the α and β bands cross E_F along the Γ-Y direction, the bottom (top) of the α (β) band locates below (above) E_F at the Γ (Γ′) point. Therefore, the α and β' bands have to overlap with each other at the Γ point as reproduced by first-principles calculations [Fig. 1(j)]. The α band bottom is ∼100 meV below E_F, in the same order of energy resolution of SX-ARPES measurements. Although we cannot clearly resolve the parabolic dispersion within this small energy window, the DFT calculations show an overall agreement with SX-ARPES results [Figs. 1(i) and 1(j)]. The band inversion between the α and β' bands around the Γ point leads to a nodal ring in the $k_x = 0$ plane (labeled as NR_x), which is protected by $\widetilde{M}_x$ when SOC is not included (as seen from Figs. S1 and S2 in the Supplemental Material [62]).

Along the Γ-X direction, the α' and β' bands can be resolved in the second BZ; they are quite close to each other near E_F and well separated at $E_B > 0.2$ eV. Similarly, because both the $\alpha'$and β' bands cross E_F, we can ascertain that the β' band crosses with the α band with missing spectra weight near the X point, forming a nodal chain touching at the S points in the $k_y = 0$ plane (labeled as NC_y), which is guaranteed by nonsymmorphic symmetries as discussed in detail later.

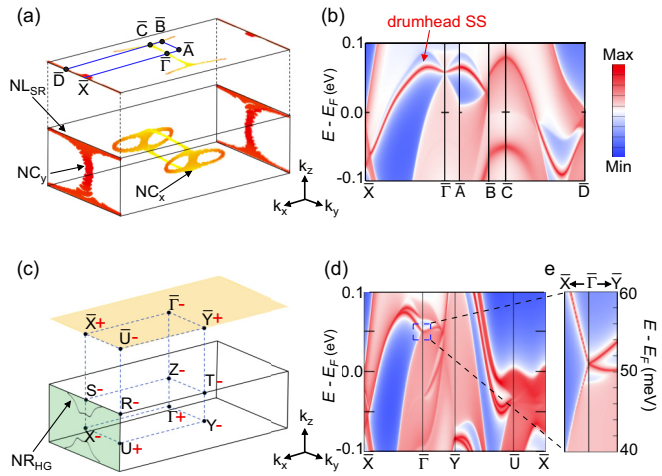

FIG. 2. (a) The bulk nodes and their surface projections in Nb_3SiTe_6 from calculations without SOC. (b) The calculated spectra weight on the (001) surface, along the momentum path passing through the projections of nodes as indicated in (a). (c) The calculated parity of time-reversal invariant momentum points in the bulk and surface Brillouin zones, as SOC is taken into account. (d) The spectra weight on the (001) surface derived from calculations with SOC. (e) A zoomed-in area in (d).

Figure 2(a) summarizes the nodes composed by the α/α' and β/β' bands when SOC is not included. First-principles calculations further unveil two more nodal rings touching with NR_x and forming a nodal chain with a finite length (NC_x). Topological drumhead surface states are shown in the calculated spectra function on the (001) surface [Fig. 2(b)], with the boundary bonding to surface projections of the nodes. The drumhead states are fourfold degenerated (including the spin degeneracy), because each point on the nodal chain projections line corresponds to two nodes with $\pm k_z$ in the three-dimensional (3D) BZ. This is consistent with previous theoretical study on topological nodal chain semimetal IrF_4 [63].

In the presence of SOC, the nodal line and chains are gapped, however, in two distinct ways. SOC gaps NL_{SR} as described in Fig. 1(d), with hourglass nodes forming rings NR_{HG} surrounding the S points in Fig. 2(c) (more details discussed in Figs. S3 and S4 in the Supplemental Material [62]). For NC_x and NC_y, SOC fully gaps the nodes and results in a TI scenario as described in Fig. 1(c). Parity calculations indicate Z_2 indices of {0;110} in a weak TI configuration with band inversion happening at the Γ and U points [Fig. 2(c)]. Topological surface states related to the weak TI phase emerge on the (001) surface [Fig. 2(d)]. Compared to the calculation without SOC, the bulk band projections open a gap at the $\bar{\Gamma}$ point, and a pair of Dirac cones appears inside the gap with Dirac points close to the bulk valence and conduction bands, respectively [Fig. 2(e)]. We note that $\widetilde{M}_y$ is preserved on the $\bar{\Gamma}$-$\bar{X}$ path near the (001) surface region; therefore along the $\bar{\Gamma}$-$\bar{X}$ direction such a dual Dirac-cone structure is an effective hourglass dispersion as imposed by $\widetilde{M}_y$.

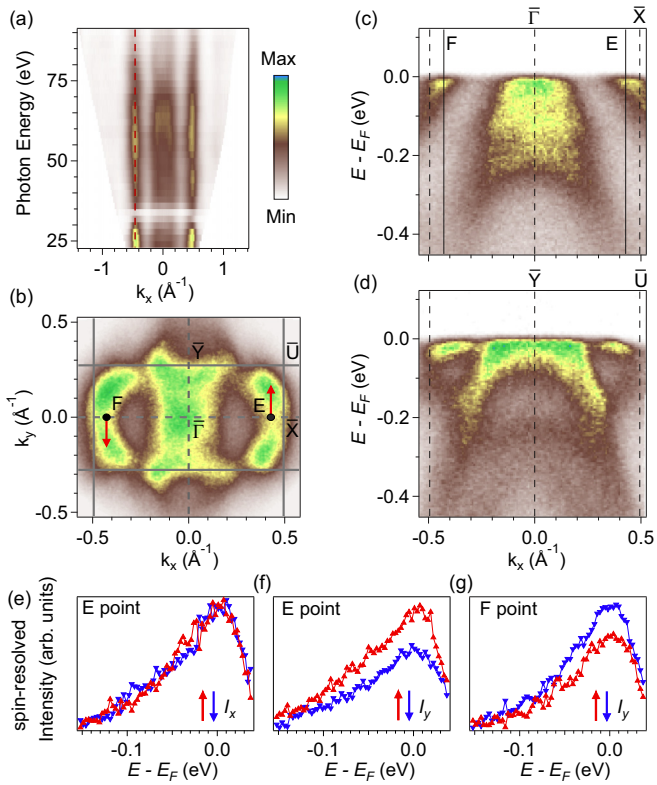

FIG. 3. (a) Photon energy dependent ARPES results at E_F of Nb_3GeTe_6 along the $\bar{\Gamma}$-$\bar{X}$ direction. (b) Fermi surface mapping of Nb_3GeTe_6. (c), (d) Photoemission intensity plots along the $\bar{\Gamma}$-$\bar{X}$ and $\bar{Y} - \bar{U}$ directions, respectively. (e) Spin-polarized EDC along the x direction ($I^{\uparrow\downarrow}{}_x$) measured at the E point as indicated in (b), (c). The red and blue curves represent the positive and negative directions, respectively. (f) Same as (e) but for the spin polarization along the y direction ($I^{\uparrow\downarrow}{}_y$). (g) Same as (f), but measured at the F point in (b), (c). (b)–(g) are measured on Nb_3GeTe_6 with 21.2 eV light.

The spin-polarized topological surface states is directly observed in our spin-resolved VUV-ARPES measurements on Nb_3GeTe_6, which shares a similar electronic structure with Nb_3SiTe_6 (Fig. S5 in the Supplemental Material [62]). In Fig. 3(a), we clearly identify a band near the $\bar{X}$ point showing no dispersion with photon energy in the range of 24–90 eV, which conforms the two-dimensional (2D) surface-state nature. We plot the Fermi surface (FS) mapped in the surface BZ [Fig. 3(b)]. Figures 3(c) and 3(d) display the surface band structure along the $\bar{\Gamma}$-$\bar{X}$ and $\bar{Y}$-$\bar{U}$ directions, respectively, in which additional spectra weight appears near E_F around the $\bar{X}$ and $\bar{U}$ points, in good agreement with the topological surface state indicated by calculations in Fig. 2(d).

We performed spin-resolved ARPES measurements to study the spin texture of the surface states. We note that the upper branch of the lower Dirac cone (DC_l) and lower branch of the upper Dirac cone (DC_U) are quite close to each other near the $\bar{X}$ point [Fig. 2(d)] and the spin signals would be mixed by limited experimental resolution. To avoid this complexity, we focus on the surface states along the $\bar{\Gamma}$-$\bar{X}$ direction in which only single Dirac cone dispersion has nonzero spectra weight in an ARPES experiment, due to the selection rule related to $\widetilde{M}_y$. Figures 3(e) and 3(f) show the spin-resolved energy distribution curve (EDC) intensity $I^{\uparrow\downarrow}{}_{x,y}$ in the x and y directions, respectively, measured at the E point labeled in Figs. 3(b) and 3(c). While $I^{\uparrow}{}_x$ is almost equal to $I^{\downarrow}{}_x$ [Fig. 3(e)], there is a clear difference in $I^{\uparrow}{}_y$ and $I^{\downarrow}{}_y$ at the EDC's peak that corresponds to surface states [Fig. 3(f)], indicating that the observed surface state is spin polarized along the y direction. At the time-reversal symmetric F point labeled in Figs. 3(b) and 3(c), the surface state is spin polarized along the y direction [Fig. 3(g)], however, in the opposite direction to that at the E point. Our spin-resolved VUV ARPES clearly reveals the topological surface states with spin-momentum locking as evidence of inherited weak TI phase in Nb_3XTe_6.

The bulk bands of Nb_3XTe_6 are spin degenerated as required by time-reversal and inversion symmetries. The "hidden" spin signals from the bulk projection bands, as observed in systems with both time-reversal and inversion symmetries [64,65], are forbidden along the $\bar{\Gamma}$-$\bar{X}$ direction by symmetries of Nb_3XTe_6 monolayer (Fig. S6 in the Supplemental Material [62]). Therefore, spin polarization observed in Figs. 3(e)–3(g) is from topological surface states, without contribution from bulk band projections.

IV. DISCUSSIONS

Figure 4 schematically summarizes our main finding of the electronic structure and topological properties of Nb_3XTe_6. From SX-ARPES results in Fig. 1, we directly observe the bulk α and β bands overlap with each other near E_F and form nodal line NL_{SR} and nodal chains NC_x/NC_y if ignoring SOC [Fig. 4(a)]. A topological drumhead state emerges on the (001) surface, bonding to the surface projections of nodes [Fig. 4(b)]. In contrast to the nodal line/chain induced by band overlap without symmetry protection as depicted in Figs. 1(a) and 1(b), NC_y is essential and based on a band inversion [Fig. 1(k)] guaranteed by nonsymmorphic symmetries, as illustrated by Figs. 4(c) and 4(d). Because the $k_y = 0$ plane, which hosts the nodal chain NC_y [yellow plane in Figs. 4(a) and (c)], is the invariant plane of $\widetilde{M}_y$, for each band $|u\rangle$ we have

$$\widetilde{M}_y|u\rangle = g_{\widetilde{M}_y}|u\rangle.$$

Because of nonprimitive translation operations, $\widetilde{M}_y$ takes eigenvalues of

$$g_{\widetilde{M}_y} = \pm e^{-\frac{ik_x a}{2}},$$

when SOC is not included. We now consider band structure along the path of K-Γ-Q in Fig. 4(c), where $K = (\pi, 0, k_z)$ and $Q = (k_x, 0, \pi)$ are arbitrary points sitting on the X-S and S-Z high-symmetry lines, respectively. The solid and dashed lines in Fig. 4(d) distinguish the additional phase term (–1) in $g_{\widetilde{M}_y}$. Because the K point on the X-S high-symmetry line is invariant under $\widetilde{M}_x$, and the commutation relationship between $\widetilde{M}_x$ and $\widetilde{M}_y$ is

$$\widetilde{M}_y\widetilde{M}_x = T_{1\bar{1}0}\widetilde{M}_x\widetilde{M}_y,$$

where $T_{1\bar{1}0}(x,\ y,\ z) = (x + a,\ y - b,\ z)$,

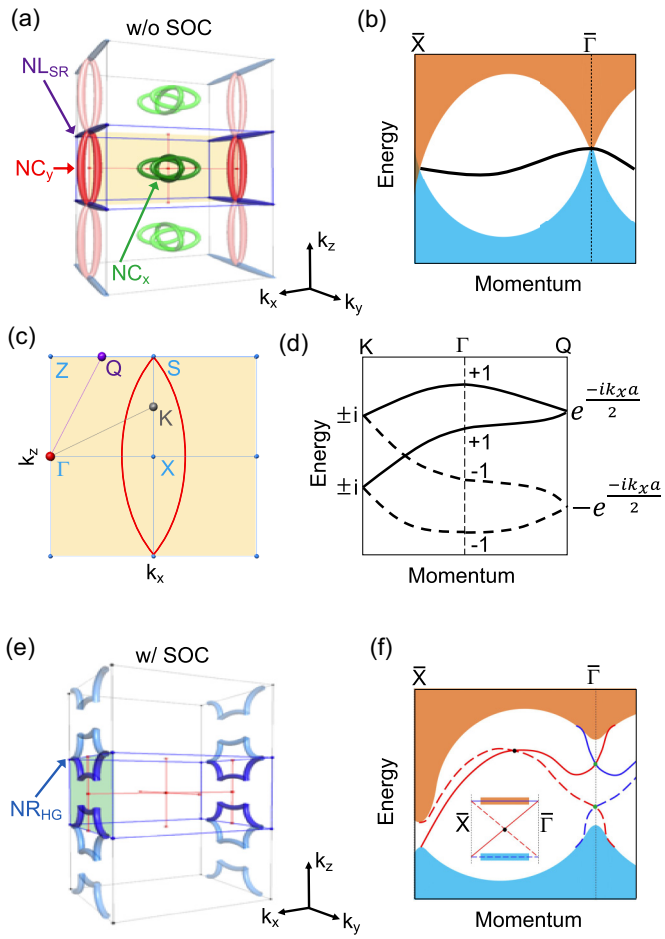

FIG. 4. (a), (b) Schematic drawings of Dirac nodal line/chains and topological surface states, respectively. (c) Dirac nodal chain NC_y in the $k_y = 0$ plane. (d) Band structure without SOC along the K-Γ-Q direction, with the eigenvalues of $\widetilde{M}_y$ labeled. (e) Hourglass nodal ring as SOC is included. (f) Topological surface states as inherited signature of weak TI phase.

the bands with additional phase term have to degenerate at the K point with the opposite of eigenvalues of $\pm i$ in Fig. 4(d):

$$\widetilde{M}_y\widetilde{M}_x|u\rangle_K = e^{-ik_xa}\widetilde{M}_x\widetilde{M}_y|u\rangle_K = -g_{\widetilde{M}_y}\widetilde{M}_x|u\rangle_K.$$

Because there are two layers in the unit cell of Nb_3XTe_6 [Fig. 1(e)] and the interlayer coupling strength is considerable [Fig. 1(g)], the interlayer splitting has to be taken into account in Fig. 4(d). The double degeneracy on the S-Z high-symmetry line is guaranteed by $T\tilde{C}_{2z}$ symmetry, where $\tilde{C}_{2z}$ is a screw rotation along the z direction; i.e.,

$$\tilde{C}_{2z}(x, y, z) \to (-x, -y, z + 1/2c).$$

At the $k_z = \pi$ plane which includes the S-Z path and is invariant under $T\tilde{C}_{2z}$, $(T\tilde{C}_{2z})^2 = -1$ ensures each band to be Kramers doubly degenerate. Also, by noting

$$\begin{aligned}\widetilde{M}_y(T\tilde{C}_{2z}) &= T_{110}(T\tilde{C}_{2z})\widetilde{M}_y\\ &= e^{-i(k_xa+k_yb)}(T\tilde{C}_{2z})\widetilde{M}_y\\ &= e^{-i(k_xa)}(T\tilde{C}_{2z})\widetilde{M}_y,\end{aligned}$$

along the S-Z line, each Kramers pair at the Q point must share the same $\widetilde{M}_y$ eigenvalue, as imposed by

$$\widetilde{M}_y(T\tilde{C}_{2z})|u\rangle_Q = e^{-i(k_xa)}(T\tilde{C}_{2z})\widetilde{M}_y|u\rangle_Q = g_{\widetilde{M}_y}(T\tilde{C}_{2z})|u\rangle_Q,$$

where $g_{\widetilde{M}_y} = e^{-\frac{ik_xa}{2}}$ or $-e^{-\frac{ik_xa}{2}}$.

Thus, the band dispersion along the K-Γ-Q path effectively forms an hourglass dispersion, with the hourglass node with opposite $g_{\widetilde{M}_y}$ values guaranteed by nonsymmorphic symmetries. It is different from band inversion without symmetry protection as described in Fig. 1(b). By tuning hopping parameters, the band inversion along the Γ-K direction can be lifted and the hourglass nodes will be shifted to the Γ-Q direction but cannot be eliminated without breaking the nonsymmorphic symmetries (Fig. S7 in the Supplemental Material [62]).

The considerable strength of SOC in Nb_3XTe_6 eventually gaps the nodal line and chains in Fig. 4(a) in two ways. As protected by $\widetilde{M}_x$, SOC turns NL_{SR} into an hourglass nodal ring NR_{HG} [Fig. 4(e)]. In contrast, SOC fully gaps NC_x and NC_y and results in a weak TI phase with $Z_2 = \{0; 110\}$. Topological drumhead surface states evolve into a pair of spin-split Dirac cones at the $\bar{\Gamma}$ point in Fig. 4(f). Such a dual Dirac-cone structure is effectively an hourglass dispersion along the $\bar{\Gamma}$-$\bar{X}$ direction, because the $\widetilde{M}_y$ is preserved on the $\bar{\Gamma}$-$\bar{X}$ path. The upper branches of the two Dirac cones have to be degenerated at the $\bar{X}$ point as required by time-reversal symmetry, through the bulk conduction bands. Similarly, the lower branches of the Dirac cones have to be degenerated at the $\bar{X}$ point through the bulk valence bands. An hourglass node is formed and guaranteed by $\widetilde{M}_y$ [inset of Fig. 4(f)]. The spin-polarized topological surface state, as the signature of a weak TI phase, are observed in spin-resolved VUV-ARPES measurements in Fig. 3, coexisting with bulk hourglass fermions.

Therefore, we uncover a unique topological phase in Nb_3XTe_6, which shows a full set of fingerprints of weak TI and hourglass TSM phases near E_F, derived from the same group of valence and conduction bands in a single material. The inherited TI signatures are stable and guaranteed by nonsymmorphic symmetries, in contrast to that induced by band inversion without symmetry protection. The unique behaviors of the topological hourglass surface state on the (001) surface with a narrow bandwidth inherited from the weak TI phase and the interactions with homological bulk hourglass fermions call for further research activities. Considering the compositional-tunable nature of the layered vdW NbX_nTe_2 family [66] and 1D massless Dirac fermions observed in $NbSi_{0.45}Te_2$ [46], our results also unveil a promising platform for tuning the hourglass fermions and topological phase transition with multiple parameters such as thickness and X stoichiometry.

ACKNOWLEDGMENTS

This work was supported by the Ministry of Science and Technology of China (Grant No. 2018YFA0307000), Chinese National Key Research and Development Program (Grants No. 2018FYA0305800, No. 2017YFA0302901, and No. 2016YFA0300604), the National Natural Science Foundation of China (Grants No. U2032128, No. U2032204, No. 11874047, No. 92065201, and No. 11790313),

Singapore Ministry of Education AcRF Tier 2 (Grants No. MOE2019-T2-1-001), and the Strategic Priority Research Program (B) of the Chinese Academy of Sciences (Grant No. XDB33000000).

[1] K. V. Klitzing, G. Dorda, and M. Pepper, New Method for High-Accuracy Determination of the Fine-Structure Constant Based on Quantized Hall Resistance, Phys. Rev. Lett. **45**, 494 (1980).

[2] D. J. Thouless, M. Kohmoto, M. P. Nightingale, and M. den Nijs, Quantized Hall Conductance in a Two-Dimensional Periodic Potential, Phys. Rev. Lett. **49**, 405 (1982).

[3] M. Kohmoto, Topological invariant and the quantization of the hall conductance, Ann. Phys. **160**, 343 (1985).

[4] X. G. Wen, Topological orders in rigid states, Int. J. Mod. Phys. B **4**, 239 (1990).

[5] X. G. Wen, Theory of the edge states in fractional quantum Hall effects, Int. J. Mod. Phys. B **6**, 1711 (1992).

[6] M. Z. Hasan and C. L. Kane, Colloquium: Topological insulators, Rev. Mod. Phys. **82**, 3045 (2010).

[7] X. L. Qi and S. C. Zhang, Topological insulators and superconductors, Rev. Mod. Phys. **83**, 1057 (2011).

[8] J. E. Moore and L. Balents, Topological invariants of time-reversal-invariant band structures, Phys. Rev. B **75**, 121306(R) (2007).

[9] C. L. Kane and E. J. Mele, Z_2 Topological Order and the Quantum Spin Hall Effect, Phys. Rev. Lett. **95**, 146802 (2005).

[10] C. L. Kane and E. J. Mele, Quantum Spin Hall Effect in Graphene, Phys. Rev. Lett. **95**, 226801 (2005).

[11] B. A. Bernevig, T. L. Hughes, and S. C. Zhang, Quantum spin Hall effect and topological phase transition in HgTe quantum wells, Science **314**, 1757 (2006).

[12] M. König, S. Wiedmann, C. Brüne, A. Roth, H. Buhmann, L. W. Molenkamp, X. L. Qi, and S. C. Zhang, Quantum spin Hall insulator state in HgTe quantum wells, Science **318**, 766 (2007).

[13] L. Fu and C. L. Kane, Topological insulators with inversion symmetry, Phys. Rev. B **76**, 045302 (2007).

[14] C. L. Kane and E. J. Mele, A new spin on the insulating state, Science **314**, 1692 (2006).

[15] H. J. Zhang, C. X. Liu, X. L. Qi, X. Dai, Z. Fang, and S. C. Zhang, Topological insulators in Bi_2Se_3, Bi_2Te_3 and Sb_2Te_3 with a single Dirac cone on the surface, Nat. Phys. **5**, 438 (2009).

[16] Y. L. Chen, J. G. Analytis, J. H. Chu, Z. K. Liu, S. K. Mo, X. L. Qi, H. J. Zhang, D. H. Lu, X. Dai, Z. Fang, S. C. Zhang, I. R. Fisher, Z. Hussain, and Z. X. Shen, Experimental realization of a three-dimensional topological insulator, Bi_2Te_3, Science **325**, 178 (2009).

[17] N. P. Armitage, E. J. Mele, and Ashvin Vishwanath, Weyl and Dirac semimetals in three-dimensional solids, Rev. Mod. Phys. **90**, 015001 (2018).

[18] Z. J. Wang, Y. Sun, X. Q. Chen, C. Franchini, G. Xu, H. Weng, X. Dai, and Z. Fang, Dirac semimetal and topological phase transitions in A_3Bi (A = Na, K, Rb), Phys. Rev. B **85**, 195320 (2012).

[19] Z. K. Liu, B. Zhou, Y. Zhang, Z. J. Wang, H. M. Weng, D. Prabhakaran, S.-K. Mo, Z. X. Shen, Z. Fang, X. Dai, Z. Hussain, and Y. L. Chen, Discovery of a three-dimensional topological Dirac semimetal, Na_3Bi, Science **343**, 864 (2014).

[20] M. Neupane, S. Y. Xu, R. Sankar, N. Alidoust, G. Bian, C. Liu, I. Belopolski, T. R. Chang, H. T. Jeng, H. Lin, A. Bansil, F. Chou, and M. Z. Hasan, Observation of a three-dimensional topological Dirac semimetal phase in high-mobility Cd_3As_2, Nat. Commun. **5**, 3786 (2014).

[21] S. Borisenko, Q. Gibson, D. Evtushinsky, V. Zabolotnyy, B. Buchner, and R. J. Cava, Experimental Realization of a Three-Dimensional Dirac Semimetal, Phys. Rev. Lett. **113**, 027603 (2014).

[22] J. Xiong, S. K. Kushwaha, T. Liang, J. W. Krizan, M. Hirschberger, W. Wang, R. J. Cava, and N. P. Ong, Evidence for the chiral anomaly in the Dirac semimetal Na_3Bi, Science **350**, 413 (2015).

[23] L. M. Schoop, M. N. Ali, C Straer, A. Topp, A. Varykhalov, D. Marchenko, V. Duppel, S. S. P. Parkin, B. V. Lotsch, and C. R. Ast, Dirac cone protected by non-symmorphic symmetry and three-dimensional Dirac line node in ZrSiS, Nat. Commun. **7**, 11696 (2016).

[24] H. M. Weng, Y. Y. Liang, Q. N. Xu, R. Yu, Z. Fang, X. Dai, and Y. Kawazoe, Topological node-line semimetal in three-dimensional graphene networks, Phys. Rev. B **92**, 045108 (2015).

[25] R. Yu, H. M. Weng, Z. Fang, X. Dai, and X. Hu, Topological Node-Line Semimetal and Dirac Semimetal State in Antiperovskite Cu_3PdN, Phys. Rev. Lett. **115**, 036807 (2015).

[26] G. Bian, T.-R. Chang, R Sankar, S.-Y. Xu, H. Zheng, T. Neupert, C-K Chiu, S.-M. Huang, G. Q. Chang, I. Belopolski1, D. S. Sanchez, M. Neupane, N. Alidoust, C. Liu, B. K. Wang, C.-C. Lee, H.-T. Jeng, C. L. Zhang, Z. J. Yuan, S. Jia *et al.*, Topological nodal-line fermions in spin-orbit metal $PbTaSe_2$, Nat. Commun. **7**, 10556 (2016).

[27] J. Hu, Z. J. Tang, J. Y. Liu, X. Liu, Y. L. Zhu, D. Graf, K. Myhro, S. Tran, C. N. Lau, J. Wei, and Z. Q. Mao, Evidence of Topological Nodal-Line Fermions in ZrSiSe and ZrSiTe, Phys. Rev. Lett. **117**, 016602 (2016).

[28] X. Wan, A. M. Turner, A. Vishwanath, and S. Y. Savrasov, Topological semimetal and Fermi-arc surface states in the electronic structure of pyrochlore iridates, Phys. Rev. B **83**, 205101 (2011).

[29] G. Xu, H. Weng, Z. Wang, X. Dai, and Z. Fang, Chern Semimetal and the Quantized Anomalous Hall Effect in $HgCr_2Se_4$, Phys. Rev. Lett. **107**, 186806 (2011).

[30] H. M. Weng, C. Fang, Z. Fang, B. A. Bernevig, and X. Dai, Weyl Semimetal Phase in Noncentrosymmetric Transition-Metal Monophosphides, Phys. Rev. X **5**, 011029 (2015).

[31] S.-M. Huang, S.-Y. Xu, I. Belopolski, C.-C. Lee, G. Q. Chang, B. K. Wang, N. Alidoust, G. Bian, M. Neupane, C. L. Zhang, S. Jia, A. Bansil, H. Lin, and M. Z. Hasan, A Weyl fermion semimetal with surface Fermi arcs in the transition metal monopnictide TaAs class, Nat. Commun. **6**, 7373 (2015).

[32] B. Q. Lv, H. M. Weng, B. B. Fu, X. P. Wang, H. Miao, J. Ma, P. Richard, X. C. Huang, L. X. Zhao, G. F. Chen, Z. Fang, X. Dai, T. Qian, and H. Ding, Experimental Discovery of Weyl Semimetal TaAs, Phys. Rev. X **5**, 031013 (2015).

[33] B. Q. Lv, N. Xu, H. M. Weng, J. Z. Ma, P. Richard, X. C. Huang, L. X. Zhao, G. F. Chen, C. Matt, F. Bisti, V. N. Strocov, J. Mesot, Z. Fang, X. Dai, T. Qian, M. Shi, and H. Ding, Nat. Phys. **11**, 724 (2015).

[34] S. Y. Xu, I. Belopolski, N. Alidoust, M. Neupane, G. Bian, C. L Zhang, R. Sankar, G. Q. Chang, Z. J. Yuan, C. C. Lee, S. M. Huang, H. Zheng, J. Ma, D. S. Sanchez, B. K. Wang, A. Bansil, F. C. Chou, P. P. Shibayev, H. Lin, S. Jia *et al.*, Discovery of a Weyl fermion semimetal and topological Fermi arcs, Science **349**, 613 (2015).

[35] N. Xu, H. M. Weng, B. Q. Lv, C. Matt, J. Park, F. Bisti, V. N. Strocov, E. Pomjakushina, K. Conder, N. C. Plumb, M. Radovic, G. Autès, O. V. Yazyev, Z. Fang, X. Dai, G. Aeppli, T. Qian, J. Mesot, H. Ding, and M. Shi, Observation of Weyl nodes and Fermi arcs in tantalum phosphide, Nat. Commun. **7**, 11006 (2016).

[36] L. X. Yang, Z. K. Liu, Y. Sun, H. Peng, H. F. Yang, T. Zhang, B. Zhou, Y. Zhang, Y. F. Guo, M. Rahn, D. Prabhakaran, Z. Hussain, S. K. Mo, C. Felser, B. Yan, and Y. L. Chen, Weyl semimetal phase in the non-centrosymmetric compound TaAs, Nat. Phys. **11**, 728 (2015).

[37] N. Xu, G. Autés, C. E. Matt, B. Q. Lv, M. Y. Yao, F. Bisti, V. N. Strocov, D. Gawryluk, E. Pomjakushina, K. Conder, N. C. Plumb, M. Radovic, T. Qian, O. V. Yazyev, J. Mesot, H. Ding, and M. Shi, Distinct Evolutions of Weyl Fermion Quasiparticles and Fermi Arcs with Bulk Band Topology in Weyl Semimetals, Phys. Rev. Lett. **118**, 106406 (2017).

[38] S. Y. Xu, Y. Xia, L. A. Wray, S. Jia, F. Meier, J. H. Dil, J. Osterwalder, B. Slomski, A. Bansil, H. Lin, R. J. Cava, and M. Z. Hasan, Topological phase transition and texture inversion in a tunable topological insulator, Science **332**, 560 (2011).

[39] N. Xu, Y. T. Qian, Q. S. Wu, G. Autès, C. E. Matt, B. Q. Lv, M. Y. Yao, V. N. Strocov, E. Pomjakushina, K. Conder, N. C. Plumb, M. Radovic, O. V. Yazyev, T. Qian, H. Ding, J. Mesot, and M. Shi, Trivial topological phase of CaAgP and the topological nodal-line transition in $CaAg(P_{1-x}As_x)$, Phys. Rev. B **97**, 161111(R) (2018).

[40] N. Xu, Z. W. Wang, A. Magrez, P. Bugnon, H. Berger, C. E. Matt, V. N. Strocov, N. C. Plumb, M. Radovic, E. Pomjakushina, K. Conder, J. H. Dil, J. Mesot, R. Yu, H. Ding, and M. Shi, Evidence of a Coulomb-Interaction-Induced Lifshitz Transition and Robust Hybrid Weyl Semimetal in $T_d - MoTe_2$, Phys. Rev. Lett. **121**, 136401 (2018).

[41] S. Li, Y Liu, S. S. Wang, Z. M. Yu, S. Guan, X. L. Sheng, Y. G. Yao, and S. Y. A. Yang, Nonsymmorphic-symmetry-protected hourglass Dirac loop, nodal line, and Dirac point in bulk and monolayer X_3SiTe_6 (X = Ta, Nb), Phys. Rev. B **97**, 045131 (2018).

[42] T. Sato, Z. W. Wang, K. Nakayama, S. Souma, D. Takane, Y. Nakata, H. Iwasawa, C. Cacho, T. Kim, T. Takahashi, and Y. Ando, Observation of band crossings protected by nonsymmorphic symmetry in the layered ternary telluride Ta_3SiTe_6, Phys. Rev. B **98**, 121111(R) (2018).

[43] L. L. An, H. W. Zhang, J. Hu, X. D. Zhu, W. S. Gao, J. L. Zhang, C. Y Xi, W. Ning, Z. Q Mao, and M. L Tian, Magnetoresistance and Shubnikov–de Haas oscillations in layered Nb_3SiTe_6 thin flakes, Phys. Rev. B **97**, 235133 (2018).

[44] M. Naveed, F. C. Fei, H. J. Bu, X. Y. Bo, S. A. Shah, B. Chen, Y. Zhang, Q. Q. Liu, B. Y. Wei, S. Zhang, J. W. Guo, C. Y. Xi, A. Rahman, Z. M. Zhang, M. H. Zhang, X. G. Wan, and F. Q. Song, Magneto-transport and Shubnikov–de Haas oscillations in the layered ternary telluride topological semimetal candidate Ta_3SiTe_6, Appl. Phys. Lett. **116**, 092402 (2020).

[45] J. Hu, X. Liu, C. L. Yue, J. Y. Liu, H. W. Zhu, J. B. He, J. Wei1, Z. Q. Mao, L Yu. Antipina, Z. I. Popov, P. B. Sorokin, T. J. Liu, P. W. Adams, S. M. A. Radmanesh, L. Spinu, H. Ji, and D. Natelson, Enhanced electron coherence in atomically thin Nb_3SiTe_6, Nat. Phys. **11**, 471 (2015).

[46] T. Y. Yang, Q. Wan, D. Y. Yan, Z. Zhu, Z. W. Wang, C. Peng, Y. B. Huang, R. Yu, J. Hu, Z. Q. Mao, S. Li, S. Y. A. Yang, H. Zheng, J. F. Jia, Y. G. Shi, and N. Xu, Directional massless Dirac fermions in a layered van der Waals material with one-dimensional long-range order, Nat. Mater. **19**, 27 (2020).

[47] V. N. Strocov, X. Wang, M. Shi, M. Kobayashi, J. Krempasky, C. Hess, T. Schmitt, and L. Patthey, Soft-x-ray ARPES facility at the ADRESS beamline of the SLS: Concepts, technical realisation and scientific applications, J. Synchrotron Radiat. **21**, 32 (2014).

[48] J. P. Perdew, K. Burke, and M. Ernzerhof, Generalized Gradient Approximation Made Simple, Phys. Rev. Lett. **77**, 3865 (1996).

[49] G. Kresse and J. Hafner, *Ab initio* molecular-dynamics simulation of the liquid-metal–amorphous-semiconductor transition in germanium, Phys. Rev. B **49**, 14251 (1994).

[50] G. Kresse and J. Furthmüller, Efficient iterative schemes for *ab initio* total-energy calculations using a plane-wave basis set, Phys. Rev. B **54**, 11169 (1996).

[51] P. E. Blöchl, Projector augmented-wave method, Phys. Rev. B **50**, 17953 (1994).

[52] M. Dion, H. Rydberg, E. Schröder, D. C. Langreth, and B. I. Lundqvist, Van der Waals Density Functional for General Geometries, Phys. Rev. Lett. **92**, 246401 (2004).

[53] N. Marzari and D. Vanderbilt, Maximally localized generalized Wannier functions for composite energy bands, Phys. Rev. B **56**, 12847 (1997).

[54] I. Souza, N. Marzari, and D. Vanderbilt, Maximally localized Wannier functions for entangled energy bands, Phys. Rev. B **65**, 035109 (2001).

[55] M. P. López Sancho, J. M. López Sancho, and J. Rubio, Quick iterative scheme for the calculation of transfer matrices: Application to Mo (100), J. Phys. F **14**, 1205 (1984).

[56] M. P. López Sancho, J. M. López Sancho, and J. Rubio, Highly convergent schemes for the calculation of bulk and surface Green functions, J. Phys. F **15**, 851 (1985).

[57] Q. S. Wu, S. N. Zhang, H.-F. Song, M. Troyer, and A. A. Soluyanov, WANNIERTOOLS: An open-source software package for novel topological materials, Comput. Phys. Commun. **224**, 405 (2018).

[58] V. N. Strocov, M. Shi, M. Kobayashi, C. Monney, X. Wang, J. Krempasky, T. Schmitt, L. Patthey, H. Berger, and P. Blaha, Three-Dimensional Electron Realm in VSe_2 by Soft-X-Ray Photoelectron Spectroscopy: Origin of Charge-Density Waves, Phys. Rev. Lett. **109**, 086401 (2012).

[59] D. Pescia, A. R. Law, M. T. Johnson, and H. P. Hughes, Determination of observable conduction band symmetry in angle-resolved electron spectroscopies: Non-symmorphic space groups, Solid State Commun. **56**, 809 (1985).

[60] T. Finteis, M. Hengsberger, T. Straub, K. Fauth, R. Claessen, P. Auer, P. Steiner, and S. Hüfner, Occupied and unoccupied

electronic band structure of WSe_2, Phys. Rev. B **55**, 10400 (1997).

[61] G. Landolt, S. V. Eremeev, O. E. Tereshchenko, S. Muff, B. Slomski, K. A. Kokh, M. Kobayashi, T. Schmitt, V. N Strocov, J. Osterwalder, E. V. Chulkov, and J. H. Dil, Bulk and surface Rashba splitting in single termination BiTeCl, New J. Phys. **15**, 085022 (2013).

[62] See Supplemental Material at http://link.aps.org/supplemental/10.1103/PhysRevB.103.165107 will be inserted by publisher for Supplemental Figs. S1–S7.

[63] T. Bzdušek, Q. S. Wu, A. Rüegg, M. Sigrist, and A. A. Soluyanov, Nodal-chain metals, Nature **538**, 75 (2016).

[64] X. W. Zhang, Q. H. Liu, J. W. Luo, A. J. Freeman, and A. Zunger, Hidden spin polarization in inversion-symmetric bulk crystals, Nat. Phys. **10**, 387 (2014).

[65] J. M. Riley, F. Mazzola, M. Dendzik, M. Michiardi, T. Takayama, L. Bawden, C. Granerød, M. Leandersson, T. Balasubramanian, M. Hoesch, T. K. Kim, H. Takagi, W. Meevasana, P. Hofmann, M. S. Bahramy, J. W. Wells, and P. D. C. King, Nat. Phys. **10**, 835 (2014).

[66] Z. Zhu, S. Li, M. Yang, X. A. Nie, H. K. Xu, X. Yang, D. D. Guan, S. Y. Wang, Y. Y. Li, C. H. Liu, Z. Q. Mao, N. Xu, Y. G. Yao, S. Y. A. Yang, Y. G. Shi, H. Zheng, and J. F. Jia, A tunable and unidirectional one-dimensional electronic system $Nb_{2n+1}Si_nTe_{4n+2}$, npj Quantum Mater. **5**, 35 (2020).